Materials Science & Engineering A 941 (2025) 148655

Contents lists available at ScienceDirect

Materials Science & Engineering A

journal homepage: www.elsevier.com/locate/msea

Dual-gradient structure made a titanium alloy strong and ductile

Na Li [a,b], Yuankui Cao [a,*], Jixun Zhang [b], Jie Yan [b], Yang Ren [c], Wei Liu [a], Bin Liu [a], Yuntian Zhu [b,**], Yong Liu [a]

[a] State Key Lab of Powder Metallurgy, Central South University, Changsha, 410083, PR China
[b] Department of Materials Science and Engineering, Hong Kong Institute for Advanced Study, City University of Hong Kong, Kowloon, Hong Kong, China
[c] Department of Physics, City University of Hong Kong, Kowloon, Hong Kong, China

ARTICLE INFO

Keywords:
Titanium alloy
Mechanical property
Gradient structure
Hetero-deformation induced hardening
Stress-induced martensitic transformation

ABSTRACT

A novel binary Ti-20W alloy with precipitate-volume gradient and grain-size gradient was developed through tailoring the fluctuating distribution of W. The dual-gradient structure caused a strong hetero-deformation induced (HDI) hardening, contributing to a good combination of ultimate tensile strength of 1463 MPa and ductility (~10 %). Additionally, stress-induced martensitic transformation of $\beta \rightarrow \alpha''$ and stress/strain partitioning between α and β phases were detected by *in-situ* synchrotron X-ray diffraction, which also helped to retain a reasonable ductility.

1. Introduction

Heterostructured (HS) materials represent a category of materials designed with hard zone and soft zone, usually exhibiting superior strength-ductility synergy over homogeneous materials via producing extra hetero-deformation induced (HDI) hardening [1–3]. The successive accumulation of geometrically necessary dislocations (GNDs) near the hetero-interfaces between hard zone and soft zone is the primary mechanism for generating high HDI hardening effect [4].

Based on the mechanical continuity of interface, hetero-interfaces in HS materials can be categorized as sharp interface and gradient interface, which exhibit different capability for GNDs accumulation. Sharp interface, for example, in layered Cu-bronze materials, is typically stationary during deformation [5,6], which leads to a quick saturation of GND accumulation, and consequently limits ductility enhancement [7–9]. Gradient interface in HS materials, in contrast, migrates from softer zones to harder zones under increasing applied stress, resulting in progressive accumulation of GNDs in its wake to produce more effective and sustained HDI hardening for higher ductility. To further enlarge the benefits of gradient structures, combining multiple gradient microstructures is expected to increase the HDI hardening effect [10–13].

To date, the design of gradient HS materials mostly focuses on the surface gradient structures, such as grain-size gradient and twin gradient, and usually produces only tens of micrometers from the surface to the internal of samples [10,14]. This limits their application in thick and large components [15]. Previously, we proposed to prepare large-scale gradient Ti alloys by controlling the internal diffusion of metal particles [16,17]. A series of Ti-W alloys with the W content ranging from 5 wt% to 30 wt% were fabricated [18], where the Ti-20W alloy featured high-density hetero-interfaces and exhibited good mechanical performance [19]. Therefore, it is expected to optimize the microstructures of Ti-20W alloy to further enhance its mechanical properties.

In this study, we designed a novel gradient Ti-20W alloy by utilizing the diffusion of W, not only for its low diffusion rate that is conducive to control the Ti/W gradient interface [20], but also considering β-metastable zone induced by W diffusion where multiple deformation mechanisms may be simultaneously activated to enhance strength-ductility synergy [19]. The fluctuating distribution of W in the novel Ti-20W alloy was developed to induce a dual-gradient structure with grain-size and precipitate-volume. Such dual-gradient structure was found made the titanium alloy strong and ductile. The effects of dual-gradient structure on the mechanical properties and deformation behavior of Ti-20W alloy were investigated.

2. Materials and methods

The processing of the gradient Ti-20W alloy (weight fraction, wt.%) is schematically illustrated in Fig. S1(a). Ti powders (<43 μm) and W powders (2–4 μm) were mixed for 6 h under an argon atmosphere. The

* Corresponding author.
** Corresponding author.
E-mail addresses: caoyuankui@csu.edu.cn (Y. Cao), yuntizhu@cityu.edu.hk (Y. Zhu).

https://doi.org/10.1016/j.msea.2025.148655
Received 22 March 2025; Received in revised form 7 May 2025; Accepted 5 June 2025
Available online 6 June 2025

mixed Ti-W powder was then compacted by cold isostatic pressing at 180 MPa and subsequently sintered in a vacuum furnace at 1350 °C for 4 h to form a partially diffused Ti/W interface. The sintered billets were then extruded to elongate the W-rich structures and densify the Ti/W interface at an extension temperature of 950 °C and an extrusion ratio of 16:1, in order to obtain the fully densified Ti-20W alloy with micro-scale hetero-structures. This process fabricated cylindrical rods with a diameter of 30 mm, labeled as gradient-structured (GS) Ti-20W.

Details of the uniaxial tensile tests and loading-unloading-reloading (LUR) tests can be found in previous study [18]. Phase constituents were analyzed using X-ray diffraction (XRD). Microstructural characterization was conducted via scanning electron microscopy (SEM), transmission electron microscopy (TEM), and electron backscatter diffraction (EBSD). In-situ tensile tests were performed using synchrotron X-ray diffraction on plate-shaped GS Ti-20W tensile specimens along the extrusion direction (Fig. S1(b) and S2). Details of the in-situ tensile tests are provided in the Supplementary Material.

3. Results and discussion

The GS Ti-20W consists of α-Ti, α''-Ti, and β-Ti phases due to the dissolution of W (Fig. S3). Fig. 1(a–b) show the microstructural details in transverse and longitudinal sections of GS Ti-20W rod, respectively. The bright fiber-shaped structures aligned along the extrusion direction can be confirmed as W-rich zones by utilizing EDS analysis. These fiber-shaped W-rich zones exhibit a compositional gradient with an inter-diffusion zone of 40 μm in width (Fig. 1(c–e)), owing to the partial diffusion of W particles during sintering and subsequent severe deformation during hot extrusion. Meanwhile, microstructural differences along the compositional gradient are observed (Fig. 1(c)), which can be divided into three regions: region A (Ti-rich zone), region B (diffusion transition zone), and region C (W-rich zone), respectively. With W content increasing, a gradient structure in the size and volume of precipitates is observed in the three regions, changing from dense long lath-shaped to spare short needle-shaped morphology (Fig. 1(f–h)). Fig. 1 (i–k) show EBSD images of the GS Ti-20W, revealing a grain-size variation along the compositional gradient. Due to the high melting point of W and its restraining effect on recrystallization, the grains in the W-rich zone retained their elongated feature, while the grains away from the W-rich zone recrystallized, leading to a grain-size gradient. The KAM map shows discrepant GNDs density in W-rich and Ti-rich zones, further demonstrating the different recrystallization behavior [21]. Thus, the internal compositional gradient in the titanium alloy induced a dual-gradient structure of precipitate-volume and grain-size.

The gradient structure of precipitate-volume was further examined by TEM. In the Ti-rich zone (region A in Fig. 1(f)), the bright field (BF) image shows lath-shaped precipitates in the matrix (Fig. 2(a)). The selected area electron diffraction (SAED) pattern of the white dashed circle (SA-1) further reveals the existence of α''-Ti phase, which has an orientation relationship (OR) of $[0001]_{\alpha}//[001]_{\alpha''}//[011]_{\beta}$. The α-Ti and α''-Ti phases highlighted in the dark field (DF) images exhibit an average length of ~1.6 μm and ~0.15 μm, respectively. In the W-rich zone (region C in Fig. 1(h)), the same phase constitution and OR are also confirmed (Fig. 2(e–h)). However, the average length of α-Ti (~0.57

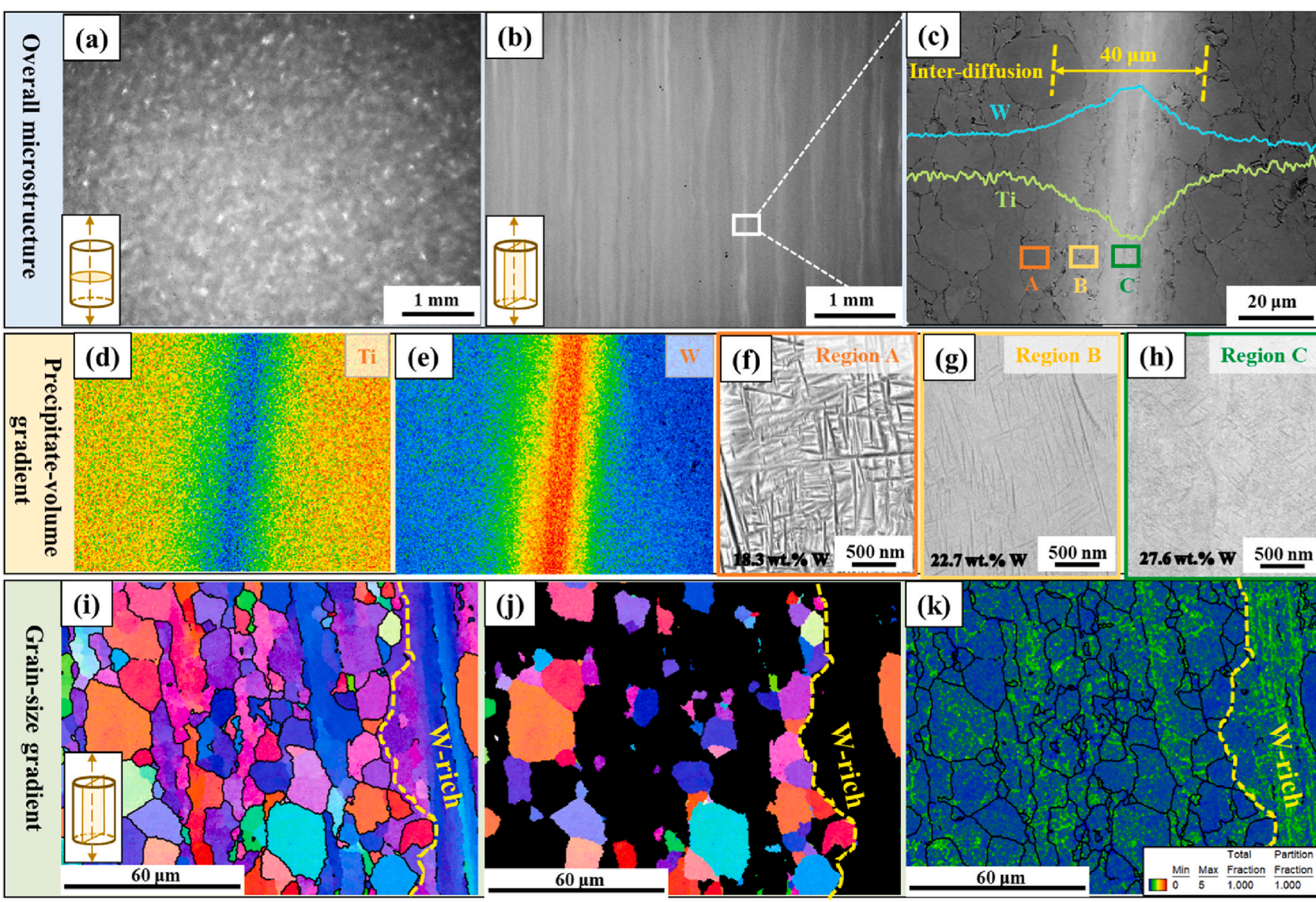

Fig. 1. Microstructures of GS Ti-20W: (a–b) Low magnification micrographs of transverse section and longitudinal section; (c) High magnification micrographs in (b) and the corresponding EDS-line scanning pattern; (d–e) Elemental distribution of Ti and W; (f–h) Local magnified images in region A, region B, and region C of (c), respectively; (i) IPF map; (j) Recrystallized grain map; (k) KAM map.

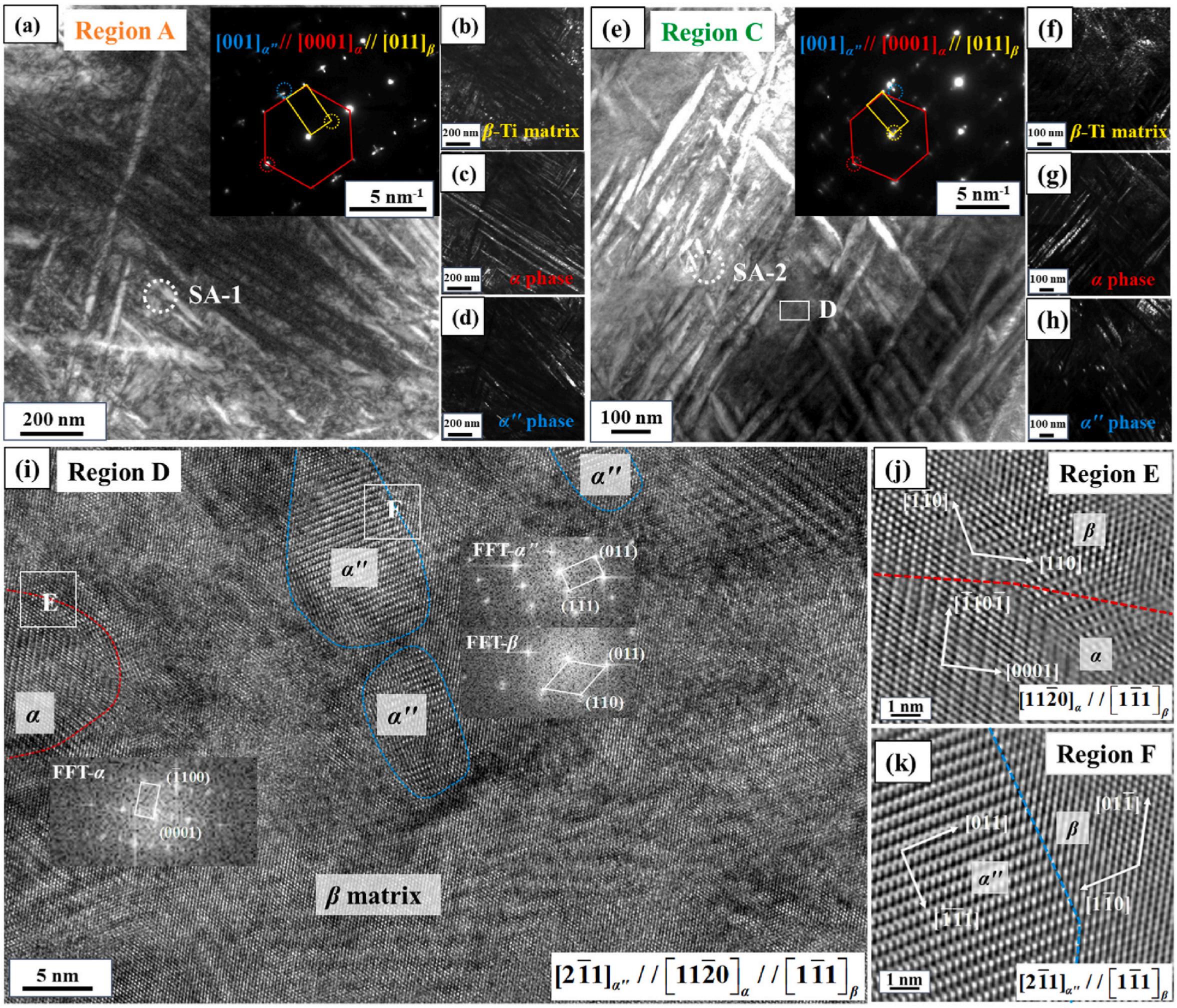

Fig. 2. TEM images of region A and region C in GS Ti-20W (Fig. 1(c)): (a)(e) Low and high magnification BF images; (b)(f) DF images of β-Ti matrix; (c)(g) DF images of α phase; (d)(h) DF images of α'' phase; and (i–k) HRTEM images of region D, E and F, respectively.

μm) and α''-Ti phase (~10 nm) in the W-rich zone is shorter than those in the Ti-rich zone, which is attributed to W dissolution. W acted as the β-stabilizer and hindered the transformation from β-Ti to α/α''-Ti phase [22], thereby reducing the size and volume fraction of precipitates. Fig. 2(i) shows the HRTEM image of the region D marked by the white rectangle in Fig. 2(e), where the zone axis is set to $[1\ \bar{1}\ 1]_\beta$. The HRTEM and Fast Fourier Transform (FFT) results indicate that the α''-Ti phase have coherent interface with the β-Ti matrix (Fig. 2(i–k)), which facilitates the dislocation accumulation and phase transformation during the deformation [23–25]. Notably, the generation of α''-Ti phase is related to the presence of metastable β-Ti phase [26]. The metastable β phase can form in case of insufficient β-stabilizing elements (such as W, Mo, etc.), which may decompose into $\alpha/\alpha'/\alpha''$ upon cooling or subjected to stress [27–29]. Therefore, it can be deduced the compositional gradient in the GS Ti-20W could produce the β-metastable phase.

Fig. 3 presents the tensile properties and post-deformation microstructures of the GS Ti-20W. The GS Ti-20W exhibits a high yield strength (YS) of 1297 MPa and ultimate tensile strength (UTS) of 1463 MPa, and also retains a reasonable elongation of 10.4 %. Fig. 3(b) summarizes the tensile properties of some high-strength titanium alloys and TMCs [19,30–33]. The GS Ti-20W alloy exhibits a better balance of strength and ductility compared to most alloys, overcoming the strength-ductility trade-off dilemma. After deformation, a pronounced difference in GNDs is observed between fiber-shaped (W-rich zone) and recrystallized (Ti-rich zone) grains (Fig. 3(c–d)). High-density GNDs are accumulated in fiber-shaped grains near the interface (as pointed out by the red arrows), leading to a high HDI stress to strengthen the GS Ti-20W alloy (Fig. S5).

The precipitation of submicron α/α'' phases and dissolution of W atoms produced the well-known precipitation strengthening and solid solution strengthening, but resulted in a limited work hardening capability. The dual-gradient structure also plays a significant role in contributing to the ultra-high strength in GS Ti-20W alloy through two aspects. Firstly, the grain-size gradient between the W-rich zone (coarse grains) and Ti-rich zone (fine grains) caused the mechanical incompatibility, which induced the generation and accumulation of GNDs in W-rich zone, and consequently strengthened the W-rich zone. Secondly, the precipitate-volume gradient between the W-rich zone (sparse and short α phases) and Ti-rich (dense and long α phases) further increased the mechanical incompatibility. The W-rich zone appeared as the soft zone, which was attributed to the increased mean free path for dislocation motion. The Ti-rich zone, on the other hand, served as hard zone. Thus, the precipitate-volume gradient also could strengthen the W-rich zone through HDI hardening. Consequently, a strong HDI strengthening effect was produced to enhance the strength of the GS Ti-20W.

In-situ synchrotron diffraction was utilized to make in-depth investigation of the deformation behavior of the GS Ti-20W sample (Fig. 4). The peak intensity of β (110) and (220) planes decrease sharply at high-stress level, together with the increase in the peak intensity of α'' (002), (221), and (004) planes (Fig. 4(a–b)). The variation for the volume fraction of β and α'' phases is quantitatively evaluated in Fig. 4(c),

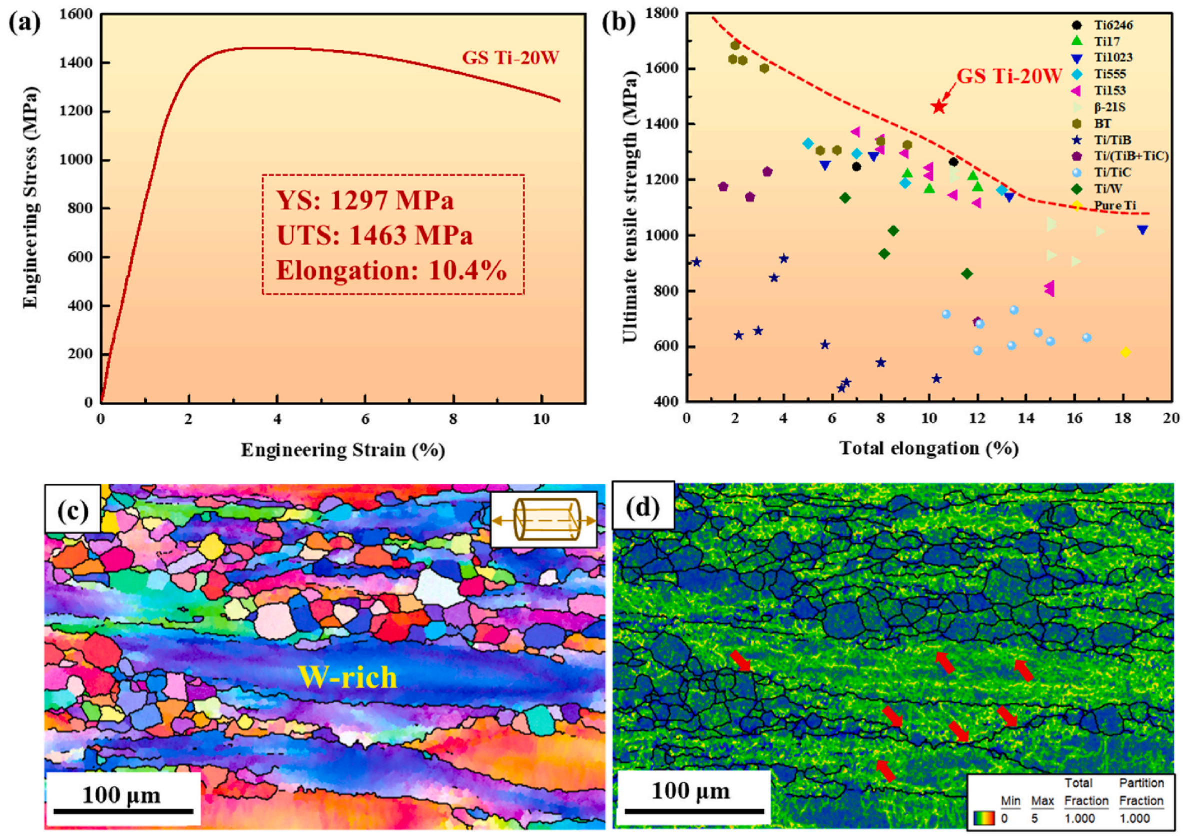

Fig. 3. (a) Engineering stress-strain curves of the GS Ti-20W; (b) Comparison of tensile properties with other high-strength Ti alloys and TMCs; EBSD analyses of GS Ti-20W near the fracture: (c) IPF map and (d) KAM map.

indicating that the stress-induced martensitic (SIM) α'' phase transformation occurred during plastic deformation. A slight fraction increase of α''-Ti at elastic stage may be induced by the fitting deviation and phase transformation [34,35]. Generally, the continuous SIM-α'' phase transformation can divide the β grain into several regions, causing dynamic Hall-Patch effect [22,36]. The SIM-α'' phases, as the deformation products, can increase the density of grain boundaries, hindering the dislocation motion. Meanwhile, the activation of SIM-α'' phase can help to relieve the local concentrated stress and coordinate the plastic strain, especially in the interface zone, thus helping to increase ductility [37].

The lattice strain and dislocation evolution of α/β phases were further investigated. The lattice strain of α and β phases along the LD and TDis calculated [38] and displayed in Fig. S7. Accordingly, the von Mises stress for α and β phase was calculated during the loading process [39], with details summarized in Supplementary Materials. As shown in Fig. 4(d), the slope of phase stress in the β-Ti phase, particularly for the β (200) and (211) families, increases after the applied stress reaching approximately 1200 MPa (near the yielding point). In the plastic deformation region, the phase stress in the β-Ti phase gradually becomes dominant, especially in the later stages of deformation. These observations confirm the existence of stress redistribution. Furthermore, the full width at half maximum (FWHM) related to the dislocation density of the α and β phase is calculated and plotted in Fig. 4(e). The FWHMs of α (100) and (201) grain families gradually decrease at the stress of ~1000 MPa, while the β (200) and β(220) families fluctuate and significantly increase after yielding. This indicates that the β phase undergoes more dislocation proliferation than the α phase after yielding [40], which is attributed to the hardening effect induced by nanoscale pre-exist and SIM-α'' phases in β phase [24]. Thus, such stress and strain partitioning can coordinate the plastic deformation, achieving a good combination of strength and ductility for the GS Ti-20W [41].

4. Conclusions

In summary, a novel Ti-20W alloy with internal compositional gradient was prepared by tailoring the W diffusion. The internal compositional gradient induced a dual-gradient structure with grain-size and precipitate-volume. The dual-gradient structure produced strong HDI hardening effect by successively accumulating GNDs in W-rich zones, empowering the GS Ti-20W alloy with an ultra-high strength of 1463 MPa and a good ductility. Meanwhile, the SIM-α'' transformation behavior along with stress and strain partitioning between α/β phase further contributed to the strength-ductility synergy of the GS Ti-20W alloy.

CRediT authorship contribution statement

Na Li: Writing – original draft, Investigation, Data curation. **Yuankui Cao:** Writing – review & editing, Supervision, Funding acquisition. **Jixun Zhang:** Methodology, Investigation. **Jie Yan:** Methodology, Investigation. **Yang Ren:** Methodology, Investigation. **Wei Liu:** Methodology, Investigation. **Bin Liu:** Methodology, Investigation. **Yuntian Zhu:** Writing – review & editing, Funding acquisition. **Yong Liu:** Data curation, Formal analysis.

Originality statement

I write on behalf of myself and all co-authors to confirm that the results reported in the manuscript are original and neither the entire work, nor any of its parts have been previously published. The authors confirm that the article has not been submitted to peer review, nor has been accepted for publishing in another journal. The authors confirm that the research in their work is original, and that all the data given in the article are real and authentic. If necessary, the article can be

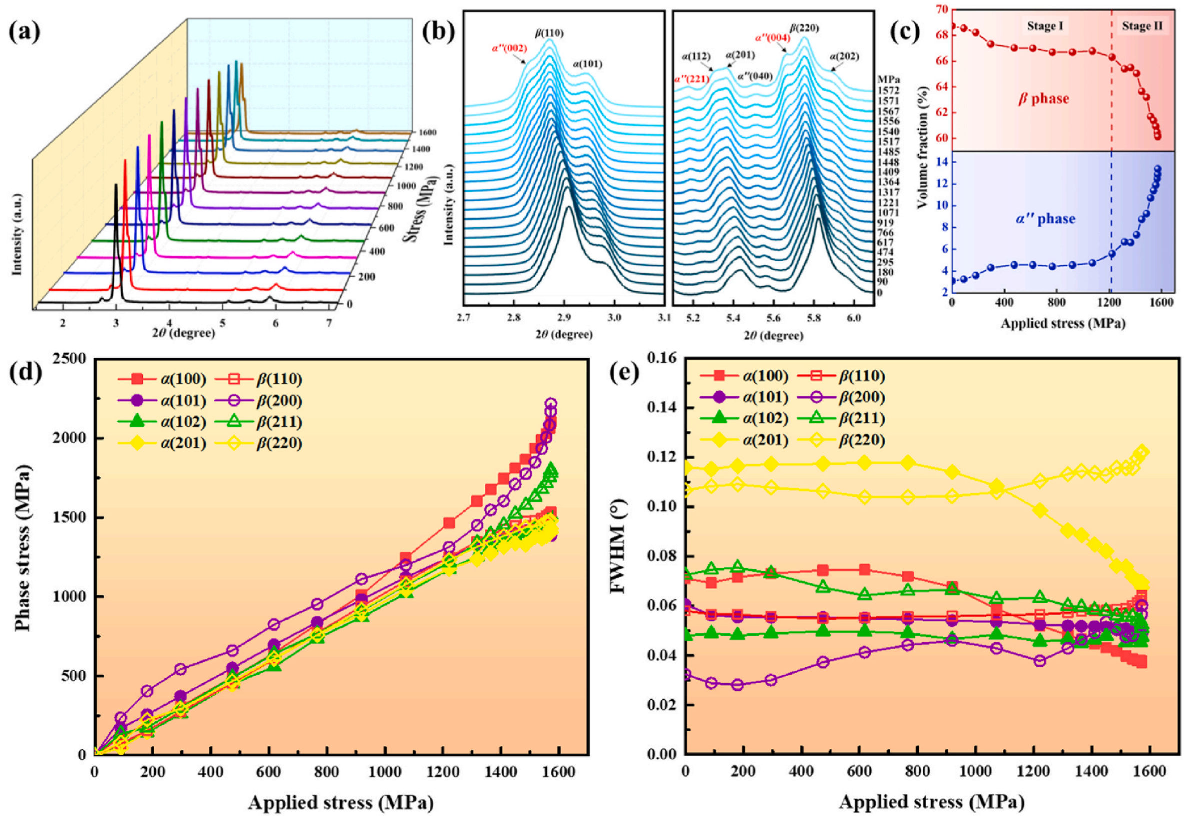

Fig. 4. (a–b) *In-situ* synchrotron X-ray diffraction patterns of GS Ti-20W along the LD under different applied stress condition; (c) Variations for the volume fraction of β and α'' phases; (d) Von Mises stress in different lattice planes; (e) FWHM versus applied stress.

recalled, and errors corrected.

Declaration of competing interest

The authors declare that they have no known competing financial interests or personal relationships that could have appeared to influence the work reported in this paper.

Acknowledgements

This work is supported by the National Key R&D Program of China (2021YFA1200202) and the Science and Technology Innovation Program of Hunan Province [No. 2024RC3001]. This research used resources of the Advanced Photon Source, a US Department of Energy (DOE) Office of Science user facility, operated for the DOE Office of Science by Argonne National Laboratory under Contract No. DE-AC0206CH11357.

Appendix A. Supplementary data

Supplementary data to this article can be found online at https://doi.org/10.1016/j.msea.2025.148655.

Data availability

The authors do not have permission to share data.

References

[1] Z.X. Shang, T.Y. Sun, J. Ding, N.A. Richter, N.M. Heckman, B.C. White, B.L. Boyce, K. Hattar, H.Y. Wang, X.H. Zhang, Sci. Adv. 9 (22) (2023) eadd9780.
[2] M. Hao, P. Li, X. Li, T. Zhang, D. Wang, Q. Sun, L. Liu, J. Li, Y. Cui, R. Yang, D. Xu, J. Mater. Sci. Technol. 124 (2022) 150–163.
[3] X.L. Wu, M.X. Yang, F.P. Yuan, G.L. Wu, Y. Wei, X. Huang, Y.T. Zhu, Proc. Natl. Acad. Sci. USA 112 (47) (2015) 14501.
[4] Y.T. Zhu, K. Ameyama, P.M. Anderson, I.J. Beyerlein, H.J. Gao, H.S. Kim, E. Lavernia, S. Mathaudhu, H. Mughrabi, R.O. Ritchie, N. Tsuji, X.Y. Zhang, X. L. Wu, Mater. Res. Lett. 9 (1) (2021) 1–31.
[5] H. Zhou, C.X. Huang, X.C. Sha, L.R. Xiao, X.L. Ma, H.W. Höppel, M. Göken, X. L. Wu, K. Ameyama, X.D. Han, Y.T. Zhu, Mater. Res. Lett. 7 (9) (2019) 376–382.
[6] A. Gryguc, S.B. Behravesh, H. Jahed, M. Wells, B. Williams, R. Gruber, A. Duquett, T. Sparrow, M. Lambrou, X. Su, Fracture and structural integrity 15 (55) (2020) 213–227.
[7] Y.T. Zhu, X.L. Wu, Prog. Mater. Sci. 131 (2023) 101019.
[8] A. Gryguc, S.B. Behravesh, S.K. Shaha, H. Jahed, M. Wells, B. Williams, X. Su, Int. J. Fatig. 116 (2018) 429–438.
[9] A. Gryguć, S.B. Behravesh, S.K. Shaha, H. Jahed, M. Wells, B. Williams, X. Su, Int. J. Fatig. 127 (2019) 324–337.
[10] Z. Cheng, H. Zhou, Q. Lu, H. Gao, L. Lu, Science. 362 (6414) (2018) eaau1925.
[11] X.T. Fang, Z.K. Li, Y.F. Wang, M. Ruiz, X.L. Ma, H.Y. Wang, Y. Zhu, R. Schoell, C. Zheng, D. Kaoumi, Y.T. Zhu, J. Mater. Sci. Technol. 98 (2022) 244–247.
[12] S. Qin, M.X. Yang, P. Jiang, J. Wang, X.L. Wu, H. Zhou, F.P. Yuan, Acta Mater. 230 (2022) 117847.
[13] W. Sun, B. Wu, H. Fu, X.-S. Yang, X. Qiao, M. Zheng, Y. He, J. Lu, S.-Q. Shi, J. Mater. Sci. Technol. 99 (2022) 223–238.
[14] K. Lu, Science. 345 (6203) (2014) 1455–1456.
[15] X.Y. Li, L. Lu, J.G. Li, X. Zhang, H.J. Gao, Nat. Rev. Mater. 5 (9) (2020) 706–723.
[16] Y.K. Cao, W.D. Zhang, B. Liu, M. Song, Y. Liu, Mater. Res. Lett. 8 (7) (2020) 254–260.
[17] S.H. Xu, Y. Liu, C. Yang, H.L. Zhao, B. Liu, J.B. Li, M. Song, Mater. Sci. Eng. A. 712 (2018) 386–393.
[18] N. Li, Y.K. Cao, B. Liu, Y. Liu, Mater. Res. Lett. 10 (6) (2022) 352–359.
[19] N. Li, Y.K. Cao, A. Fu, Q. Xie, Y. Liu, B. Liu, Mater. Char. 195 (2023) 112523.
[20] S. Wang, M.Y. Xie, H.B. Huang, M. Kang, R. Liu, C. Chen, Z. Zhang, Z.H. Zhong, Y. C. Wu, J. Alloys Compd. 879 (2021) 160451.
[21] D.Y. Lin, L.Y. Xu, Y.D. Han, Y.K. Zhang, H.Y. Jing, L. Zhao, F. Minami, Intermetallics 127 (2020) 106963.
[22] F. Sun, J.Y. Zhang, M. Marteleur, C. Brozek, E.F. Rauch, M. Veron, P. Vermaut, P. J. Jacques, F. Prima, Scr. Mater. 94 (2015) 17–20.
[23] E. Takahashi, T. Sakurai, S. Watanabe, N. Masahashi, S. Hanada, Mater. Trans. 43 (12) (2002) 2978–2983.
[24] S.H. Jiang, X.Q. Xu, W. Li, B. Peng, Y. Wu, X.J. Liu, H. Wang, X.Z. Wang, Z.P. Lu, Acta Mater. 213 (2021) 116984.
[25] F. Guo, C. Zhang, Y. Zhai, Q. Cheng, M. Wang, Q. Wang, J. Liang, W. Cao, C. Huang, Mater. Sci. Eng. A. 902 (2024) 146605.

[26] S. Sadeghpour, S.M. Abbasi, M. Morakabati, A. Kisko, L.P. Karjalainen, D.A. Porter, Scr. Mater. 145 (2018) 104–108.
[27] Z. Wyatt, S. Ankem, J. Mater. Sci. 45 (18) (2010) 5022–5031.
[28] M. Marteleur, F. Sun, T. Gloriant, P. Vermaut, P.J. Jacques, F. Prima, Scr. Mater. 66 (10) (2012) 749–752.
[29] Y. Li, S. Ni, Y. Liu, M. Song, Scr. Mater. 170 (2019) 34–37.
[30] S.L. Nyakana, J.C. Fanning, R.R. Boyer, J. Mater. Eng. Perform. 14 (6) (2005) 799–811.
[31] L.C. Qi, X.L. Qiao, L.J. Huang, X. Huang, W.L. Xiao, X.Q. Zhao, Mater. Char. 155 (2019) 109789.
[32] W.G. Zhu, J. Lei, C.S. Tan, Q.Y. Sun, W. Chen, L. Xiao, J. Sun, Mater. Des. 168 (2019) 107640.
[33] F.C. Ma, J.J. Zhou, P. Liu, W. Li, X.k. Liu, D. Pan, W.J. Lu, D. Zhang, L.Z. Wu, X. Q. Wei, Mater. Char. 127 (2017) 27–34.
[34] A. Ojha, H. Sehitoglu, Shape Mem. Superelasticity 2 (1) (2016) 50–61.
[35] A. Ojha, H. Sehitoglu, Shape Mem. Superelasticity 2 (2) (2016) 180–195.
[36] K. Chen, Q.B. Fan, J.H. Yao, L. Yang, S. Xu, Y. Gao, W. Lei, J. Alloys Compd. 920 (2022) 165563.
[37] F. Sun, J.Y. Zhang, C. Brozek, M. Marteleur, M. Veron, E. Rauch, T. Gloriant, P. Vermaut, C. Curfs, P.J. Jacques, F. Prima, Mater Today, SAVE Proc. 2 (2015) S505–S510.
[38] N. Xu, S.L. Li, R.G. Li, S.J. Wang, Y.K. Wang, Y. Ren, Y.D. Wang, Metall. Mater. Trans. A. 52 (9) (2021) 3674–3683.
[39] X.Q. Zhang, L.L. Ma, Y.F. Xue, Q.B. Fan, Z.H. Nie, L. Wang, J.M. Yin, H.F. Zhang, H. M. Fu, J. Non-Cryst. Solids 436 (2016) 9–17.
[40] H. Li, Y. Liu, W.J. Zhao, B. Liu, A. Tominaga, T. Shobu, D.X. Wei, Int. J. Plast. 165 (2023) 103612.
[41] M.Q. Zhang, B. Tang, L.M. Wang, K.D. Li, B.Q. Yin, Z.S. Zhang, J.S. Li, Mater. Sci. Eng. A. 880 (2023) 145321.